2013

System Analysis of Spatial Frequency Domain Imaging for Quantitative Mapping of Surgically Resected Breast Tissues

Ashley M. Laughney
Dartmouth College

Venkataramanan Krishnaswamy
Dartmouth College

Tyler B. Rice
University of California

David J. Cuccia
Modulated Imaging Inc.

System analysis of spatial frequency domain imaging for quantitative mapping of surgically resected breast tissues

Ashley M. Laughney
Venkataramanan Krishnaswamy
Tyler B. Rice
David J. Cuccia
Richard J. Barth
Bruce J. Tromberg
Keith D. Paulsen
Brian W. Pogue
Wendy A. Wells

System analysis of spatial frequency domain imaging for quantitative mapping of surgically resected breast tissues

Ashley M. Laughney,[a]* Venkataramanan Krishnaswamy,[a] Tyler B. Rice,[b] David J. Cuccia,[c] Richard J. Barth,[d]
Bruce J. Tromberg,[b] Keith D. Paulsen,[a,e] Brian W. Pogue,[a,d] and Wendy A. Wells[f]
[a]Dartmouth College, Thayer School of Engineering, Hanover, New Hampshire 03755
[b]University of California Irvine, Beckman Laser Institute, Irvine, California 92617
[c]Modulated Imaging Inc., Irvine, California 92617
[d]Geisel School of Medicine, Department of Surgery, Lebanon, New Hampshire 03756
[e]Geisel School of Medicine, Department of Radiology, Lebanon, New Hampshire 03756
[f]Geisel School of Medicine, Department of Pathology, Lebanon, New Hampshire 03756

Abstract. The feasibility of spatial frequency domain imaging (SFDI) for breast surgical margin assessment was evaluated in tissue-simulating phantoms and in fully intact lumpectomy specimens at the time of surgery. Phantom data was evaluated according to contrast-detail resolution, quantitative accuracy and model-data goodness of fit, where optical parameters were estimated by minimizing the residual sum of squares between the measured modulation amplitude and its solutions, modeled according to diffusion and scaled-Monte Carlo simulations. In contrast-detail phantoms, a 1.25-mm-diameter surface inclusion was detectable for scattering contrast >28%; a fraction of this scattering contrast (7%) was detectable for a 10 mm surface inclusion and at least 33% scattering contrast was detected up to 1.5 mm below the phantom surface, a probing depth relevant to breast surgical margin assessment. Recovered hemoglobin concentrations were insensitive to changes in scattering, except for overestimation at visible wavelengths for total hemoglobin concentrations <15 μM. The scattering amplitude increased linearly with scattering concentration, but the scattering slope depended on both the particle size and number density. Goodness of fit was comparable for the diffusion and scaled-Monte Carlo models of transport in spatially modulated, near-infrared reflectance acquired from 47 lumpectomy tissues, but recovered absorption parameters varied more linearly with expected hemoglobin concentration in liquid phantoms for the scaled-Monte Carlo forward model. SFDI could potentially reduce the high secondary excision rate associated with breast conserving surgery; its clinical translation further requires reduced image reconstruction time and smart inking strategies. © *The Authors. Published by SPIE under a Creative Commons Attribution 3.0 Unported License. Distribution or reproduction of this work in whole or in part requires full attribution of the original publication, including its DOI.* [DOI: 10.1117/1.JBO.18.3.036012]

Keywords: spatial frequency domain imaging; modulated imaging, near-infrared spectroscopy; tissue scattering; pathology discrimination; breast conserving surgery; margin assessment.

Paper 12623RR received Sep. 19, 2012; revised manuscript received Feb. 18, 2013; accepted for publication Feb. 20, 2013; published online Mar. 22, 2013.

1 Introduction

The feasibility of spatial frequency domain imaging (SFDI) for breast surgical margin assessment was evaluated using tissue-simulating phantoms to measure quantitative accuracy and contrast-detail resolution, and fully intact surgical specimens to assess the clinical application of this acquisition geometry to surgical breast tissues. SFDI projects sinusoidal patterns of near-infrared (NIR) light onto biological tissues to quantify wide-field spectral absorption and scattering. This unique planar imaging modality was pioneered by investigators at the University of California at Irvine and commercialized by Modulated Imaging Inc. for biological imaging at a spatial resolution between coherent and diffuse optical imaging.[1] The frequency dependence of the modulation amplitude provides a sensitive measurement to uniquely separate optical

effects using analytical models of light transport; where high spatial frequencies are sensitive to short pathlength phenomenon, primarily scattering by local fluctuations in tissue morphology, and continuous illumination is sensitive to both absorption and scattering.[1] No exogenous probes were necessary for microscopic specificity, but high spatial frequencies were probed (up to 0.33 mm^{-1}) to improve sensitivity to scattering by tissue ultra-structure. The spatial frequency of the illumination pattern integrated optical parameterization with volume averaging in depth and improved signal localization—optical parameters were recovered at depths approximately 1 to 8 mm,[2] a range appropriate for surgical margin assessment.

The scattering spectrum can be exquisitely sensitive to morphological transformations perceived by pathologists when the confounding effects of multiple light scattering are minimized; this is typically achieved through local sampling of reflectance and/or polarization techniques.[3–5] Near-source sampling of reflectance by fiber-mediated probes has demonstrated specific correlation with paraffin histology, the diagnostic gold standard, and improved tissue-type discrimination because of sensitivity to the scattering phase function.[6–9] Optical coherence tomography[10] and confocal sampling geometries[11,12] have also been applied for intra-operative diagnoses, but are limited in depth

resolution by a multiple scattering background and in field of view (FOV) size (the microscopic FOV is often too small to wholly analyze lumpectomy tissues in a clinically useful timeframe). Diffuse optical tomography can be useful to quantify bulk transformations in tissue physiology over several centimeters,[13–15] but the spatial resolution corresponds to the scattering coefficient of the tissue[16] and this can be insufficient to resolve local transformations by important scattering structures (which mainly have dimensions comparable to the optical wavelength).[17] As an intermediate between coherent and diffuse optical techniques, the ability of SFDI to effectively combine widefield optical imaging with localized scattering contrast is tested.

Scattering contrast-detail and contrast-depth resolution were explored in homogeneous polymer and gelatin phantoms with embedded inclusions because recent results suggest spectroscopic scattering features exhibited less variance within pathology subtypes and was ranked as most significant to tissue-type discrimination by an iterative feature ranking algorithm in a pilot clinical study. Quantitative accuracy of the diffusion approximation and scaled-Monte Carlo models of light transport were then compared in tissue simulating phantoms with expected optical properties and finally, goodness of fit was evaluated in reflectance measures acquired from 47 lumpectomy tissues to evaluate application of these models to surgical breast tissues. The diffusion approximation is valid for highly scattering media and for large source-to-detector separations, where high photon scattering renders their transport deterministic. Transport is governed by the reduced scattering coefficient and the absorption coefficient; consequently, information pertaining to the specific phase function is lost[18] and scattering can be convolved with absorption effects if reflectance is not measured at multiple source-to-detector separations, or equivalently, at multiple spatial frequencies. Spatially resolved, analytical solutions to the steady state diffusion approximation have been derived by Farrell and Dognitz in the real and spatial-frequency domains, respectively.[19,20] These models have demonstrated utility when tailored to specific sampling geometries[21,22] and have been improved by higher order approximations to the phase function.[23] The diffusion approximation was compared to a forward model based on scaled-Monte Carlo simulations of light transport for sampling at high spatial frequency because direct Monte Carlo simulations were computationally too expensive for an iterative optimization.[1] Numerical models were generated by rescaling a single Monte Carlo simulation to extract a wide range of optical properties from spatial-frequency dependent measures, as first realized by Graaff et al.[24] and Kienle et al.[25]

The feasibility of SFDI to distinguish malignant transformations immediately *ex vivo* in the surgical environment, prior to routine pathological processing, was evaluated in four fully intact, lumpectomy tissues in order to eventually reduce the high rate of secondary excision associated with breast conserving therapy (BCT).[26] BCT, which includes local tumor excision followed by moderate dose-radiation therapy, was the treatment of choice for nearly 75% of the approximately 300,000 new breast cancer patients diagnosed in 2011.[27] Its survival rates are equivalent to those of mastectomy when surgical resection margins are negative for residual cancer,[28,29] but margins positive for residual cancer have been associated with an increased risk of local recurrence[30–32] and mortality.[33] Margin assessment is routinely performed post-operatively by paraffin histology because frozen section analysis is limited by freezing artifacts in adipose tissues.[34,35] At Dartmouth-Hitchcock Medical Center

(DHMC), colored inks are superficially applied to the resected tissue to define margins for post-operative assessment and surgical margins are re-excised if invasive tumor is detected at the margin or if ductal carcinoma *in situ* (DCIS) is detected less than 2 mm from the inked surface.[36] Tissues excised during breast conserving surgery (BCS) may include tumors up to 5 cm in diameter, surrounded by a targeted layer of grossly normal tissue that is nearly 1 cm thick. Ideally, SFDI might be used to assess the full tumor specimen in a noncontact manner, while maintaining sensitivity to malignant transformations in localized volumes.

2 Methods

2.1 Spatial Frequency Domain Imaging System

A compact SFDI system, purchased from Modulating Imaging Inc., was used to quantitatively image optical parameters at four NIR wavelengths (658, 730, 850, and 970 nm) using spatially varying light. In series, 30 spatial frequencies uniformly distributed from 0 mm^{-1} up to 0.33 mm^{-1} were projected per wavelength onto each sample using high power light-emitting diodes (LEDs), a projection system and a digital micro-mirror device. Total data acquisition (DAQ) time was 10 min on average. Structured light patterns were generated using C# code and an ALP applications program interface, MI Acquire (v1.3.12), provided by Modulated Imaging Inc. (Irvine, California). A 12-bit CCD-based camera, coregistered with the projector, captured narrow bands of spectral reflectance using interference filters. Illuminating at a small angle to normal incidence and cross-linear polarizers placed at the source and detector minimized specular reflections. Figure 1 shows the fully integrated projection and camera subsystems mounted on a z-axis post.[1,37]
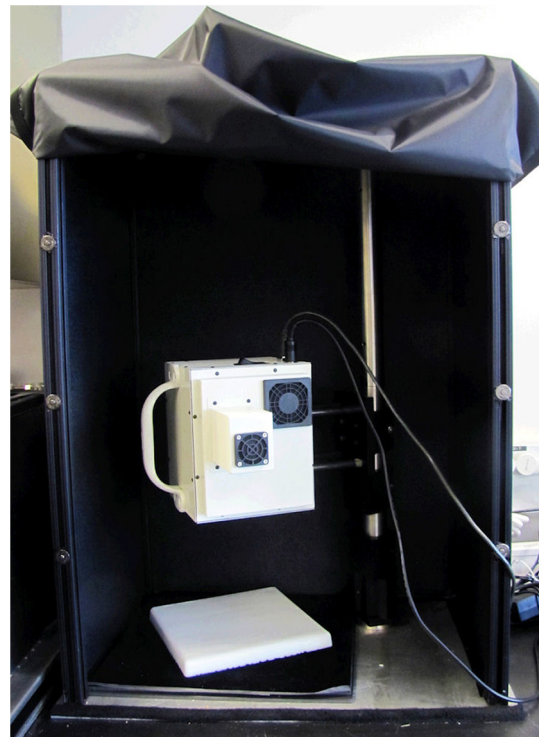

Fig. 1 Compact SFDI mounted on a z-axis post in light-shielded container; imaging a calibration standard in reflectance geometry.

2.2 Data Acquisition and Calibration

A planar and harmonically varying source illuminated each sample in reflectance geometry at normal incidence according to

$$q = q_0(z) \cos(k_x x + \alpha). \qquad (1)$$

Here, $q_0(z)$ represents the decay of the source as a function of depth in the media, α represents its phase offset, and $f_x = k_x/2\pi$ describes the spatial frequency of modulation in the x-direction. Assuming a linear medium and symmetry considerations, each sinusoidal source gave rise to a reflected intensity (I_{AC}) with the same frequency and phase:[1]

$$I_{AC}(x, y, f_x, \alpha) = M_{AC}(x, y, f_x) \cos(k_x x + \alpha). \qquad (2)$$

A three-phase demodulation was then employed to extract the frequency dependent modulation amplitude, M_{AC}, from the reflected intensity and to remove ambient noise common to all three images:[38]

$$M_{AC}(f_x) = \frac{\sqrt{2}}{3} \left[\begin{array}{l} [I_{AC}(f_x, \alpha_1) - I_{AC}(f_x, \alpha_2)]^2 + [I_{AC}(f_x, \alpha_2) - I_{AC}(f_x, \alpha_3)]^2 \\ + [I_{AC}(f_x, \alpha_3) - I_{AC}(f_x, \alpha_1)]^2 \end{array} \right]^{1/2}. \qquad (3)$$

The modulation amplitude of a siloxane titanium dioxide (TiO_2) reflectance standard with expected optical properties, $M_{AC,ref}$, was measured at each imaging session for phantom-based calibration and to correct for spatial nonuniformity in the illumination and imaging systems. The reference standard was characterized by diffuse optical spectroscopy (DOS), which combines frequency domain photon migration with broadband spectroscopy.[39] Diffuse reflectance of the standard ($R_{d,ref}$) was predicted from its expected optical properties using a forward model of light transport. Absolute reflectance of the sample (R) was subsequently calculated according to

$$R_d(f_x) = \frac{M_{AC}(f_x)}{M_{AC,ref}(f_x)} R_{d,ref}(f_x). \qquad (4)$$

Each spatial sampling point was calibrated and analyzed separately.

2.3 Comparison of Analytical Models of Reflectance

Optical parameters were fit by minimizing the residual sum of squares between the measured modulation amplitude and its analytical solution in a semi-infinite, turbid medium, modeled according to diffusion[16] and scaled-Monte Carlo simulations of light transport.[25] The former approximation assumes isotropic scattering and the latter, a Henyey-Greenstein phase function.[1] Rescaling a single, spatially and temporally resolved Monte Carlo simulation significantly reduced the computational burden associated with iterative estimation of optical parameters. However, computing its Fourier transformation was still time intensive in a minimization scheme. Consequently, scaled-Monte Carlo simulations of the modulation amplitude were stored in a 30-frequency, 4-wavelength, look up table (LUT) to reduce the computational burden associated with iterative estimation of spectral parameters. The LUT modulation amplitude was computed for absorption coefficients varying from 0 to 0.0999 mm^{-1} in steps of 1.9057E-04 mm^{-1} and scattering coefficients varying from 0.2495 to 2.1495 mm^{-1} in steps of 0.0019 mm^{-1}. A LUT was not implemented for the diffusion approximation because computation of its forward analytical solution was direct; however, other groups have implemented this to improve speed of optical parameter rendering.[1] Cuccia et al. compared the accuracy of the diffusion approximation and scaled-Monte Carlo simulation of light transport using computer simulations for a range of optical pathlengths, and showed that for low spatial frequencies in a medium with an albedo approaching 1, the diffusion error remains less than 16%.[1] Here, model-data goodness of fit was evaluated in modulated reflectance measurements acquired from 47 patients in a HIPAA-compliant, prospective study, approved by Institutional Review Board for the protection of human subjects common to evaluate the applicability of these models to light scattering in surgical breast tissues. The adjusted R^2 coefficient of determination was used to quantify data variance explained by the model and the lowest adjusted Akaike information criterion (AIC) was used to rank model performance because it is based on the negative log likelihood of the residuals and consequently, provided a relative assessment of nonlinear model fit (the R^2 coefficient of determination is known to inadequately assess nonlinear regression because the total sum of squares is not equal to the regression sum of squares, as in the linear case).[40,41] A spectrally constrained optimization was explored with the diffusion approximation given *a priori* knowledge of the chromophore extinction spectra and the wavelength-dependence of the reduced scattering coefficient. However, an unconstrained optimization was observed to be more robust given the limited number of wavelengths sampled. The ability of recovered spectral parameters to distinguish breast tissue types in this large tissue population are evaluated elsewhere; here the optimization of model-data fit is presented.

2.4 Optical Parameter Recovery

Spectral parameters were subsequently fit according to absorption by the endogenous tissue chromophores, oxygenated-hemoglobin (HbO_2), deoxygenated-hemoglobin (Hb), and water, and the wavelength-dependence of light scattering. Concentrations of HbO_2 and Hb were recast as total hemoglobin ($HbT = HbO_2 + Hb$) and percent oxygen ($\%O_2 = HbO_2/HbT$). A power law dependence on wavelength was used to describe the Mie scattering spectrum: the scattering amplitude (A) and scattering power (b) were calculated relative to the reduced scattering coefficient of 1% intralipid at $\lambda_0 = 800$ nm[42]

$$\mu_s'(\lambda) = A\mu_s'(\lambda_0)\left(\frac{\lambda}{\lambda_0}\right)^{-b}. \qquad (5)$$

Adipose was not included in the basis set of fit chromophore extinction spectra because the four wavelengths sampled were insufficient to uniquely separate water and lipid absorption; an assumption about lipid absorption was necessary during

optimization to prevent saturation of percent lipid or percent water at its bounds, as previously discussed by Mazhar.[43] Suspected lesions were primarily fibroglandular and pathology-assessed lesions were on average, 3% adipose, as determined prospectively by immunohistochemistry.

2.5 Tissue Simulating Phantoms

A homogeneous, polymer-based phantom with inclusion wells varying in diameter (1.25 to 15 mm) was custom designed and constructed by INO Inc. (*Biomimics phantom*, Quebec City, Quebec, California) for contrast-detail analysis. The absorption and reduced scattering coefficients of the phantom at 800 nm were 0.008 and 1.006 mm^{-1}, respectively; the refractive index was 1.52 and carbon black was used as an absorber. The inclusions were filled with dilutions of Intralipid, as shown in Fig. 2, to determine the minimum size of detectable scattering contrast in reduced scattering maps. Actual scattering contrast varied from 1% to 66% and was compared to measured scattering contrast; plotted along the center *x*-axis of each phantom according to:

$$\text{Contrast} = \frac{S_A - S_B}{S_A + S_B}, \qquad (6)$$

where S_A is the signal from the inclusion and S_B is the signal from the background. Sensitivity to scattering contrast at depth was additionally investigated using a gelatin phantom with scattering heterogeneities embedded 0 to 3 mm in a homogenous background, constructed with Intralipid and Nigrosin dye. Gelatin was boiled, cooled to 40°C (warm to the touch, but not solidified), and diluted with 10% Intralipid to the expected reduced scattering coefficient.[44] Inclusions were carved in the gelatin once it had cooled and were filled with another batch of liquid gelatin with greater or lower Intralipid concentration, as described by Pogue and Patterson.[45]

A series of homogenous liquid phantoms with expected optical properties were imaged to test the absolute quantification of absorption and reduced scattering coefficients by SFDI. Phantoms were constructed from Intralipid-20% (Fresenius Kabi, Uppsala, Sweden), a fat emulsion used to mimic scattering in biological tissues, diluted with phosphate buffered solution (PBS) and porcine blood.[42] PBS was used to dilute the blood to maintain blood cells at their physiological pH of 7.4. Scattering concentrations varied from 0.5% to 2.0% and the reduced scattering coefficient of each dilution was computed per wavelength according to Michels et al.[42] Initial dilutions of porcine blood were prepared using measured hematocrit values assayed with a HemoCue© meter (Hb 201 system, HemoCue Inc., Cypress, California) for each sample, and the final solution values were serially diluted from 60 to 3.75 μM, the expected physiological range in breast tissue.[46] Expected optical properties were subsequently calculated using the forward model of light transport and assuming the chromophore extinction spectra.[44] The Pearson's correlation coefficient, and coefficient of variation for all expected and recovered optical parameters were computed for model comparison. The coefficient of variation is just the standard deviation normalized to
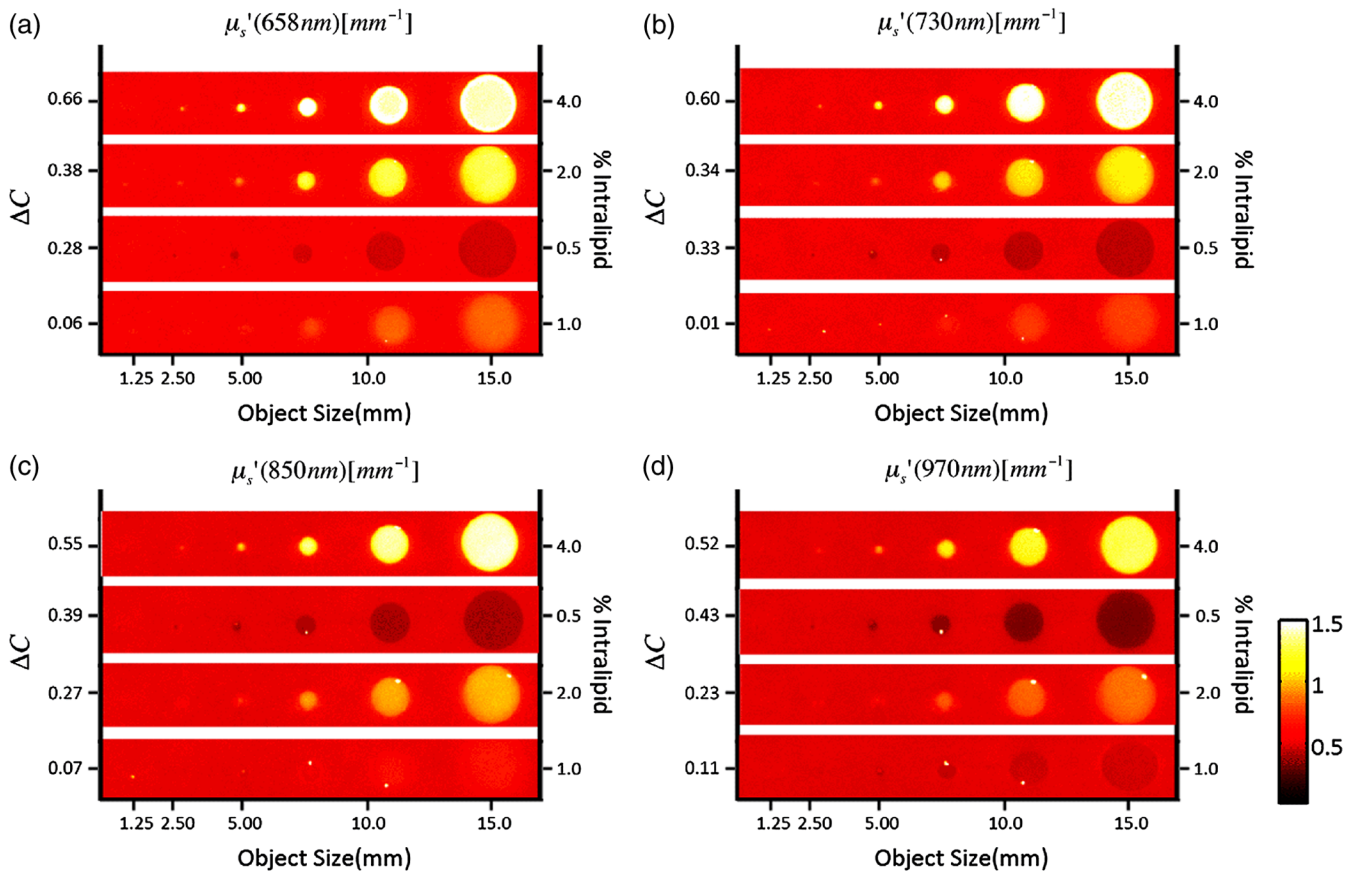

Fig. 2 Contrast-detail curves for scattering heterogeneities that vary in size (*x*-axis) and contrast (*y*-axis); measured at (a) 658 nm, (b) 730 nm, (c) 850 nm, and (d) 970 nm.

the distribution mean, and approaches 1 when two variables change together exponentially.

2.6 Spatial Frequency Domain Imaging of Lumpectomies

Four fully intact and un-inked lumpectomy specimens were imaged immediately upon excision at the time of primary surgery to test the clinical translation of this new technology. The surgeon participated in each imaging session and placed sutures in the excised tissues to safeguard knowledge of its orientation until surgical inks were applied and the tissue was sent to pathology. Fifteen spatial frequencies uniformly distributed between 0 and 0.33 mm^{-1} were projected per wavelength onto each margin in under 2 min and spectral parameters were reconstructed using the scaled-Monte Carlo LUT. Tissues were extremely malleable, so only one to three margins were imaged per specimen.

3 Results

3.1 Contrast-Detail Analysis

Maps of the reduced scattering coefficient are shown in Fig. 2 for the contrast-detail phantoms and contrast line scans are plotted in Fig. 3(a) through 3(d). Detectable scattering contrast decayed asymptotically with inclusion size, as shown in Fig. 4(a): a 1.25 mm diameter inclusion was detectable when scattering contrast was at least 28%; the lowest detectable scattering contrast was 7% when the inclusion diameter was at least 10 mm. Recovered scattering contrast was observed

to be lower than the expected scattering contrast, indicated by the dashed lines in Fig. 3(a) through 3(d), likely due to assumptions made about the optical properties of the inclusions. Figure 4(a) shows that absorption contrast, due to variations in phantom water content, was not detectable for inclusions less than 5 mm in diameter and absorption maps were characterized by a low signal-to-noise ratio (SNR). Figure 5(a) shows the reduced scattering coefficient maps for three phantoms with scattering inclusions placed at depths of 0 to 3 mm. True scattering contrast is mapped in Fig. 5(b); at least 33% scattering contrast was detectable at a 1.5 mm depth. The minimum detectable scattering contrast as a function of inclusion depth is plotted in Fig. 4(b) for the gelatin phantom; similar levels of detectable scattering contrast were observed in the polymer-based phantom. No absorption contrast was introduced into the gelatin phantom and absorption maps showed low signal to noise ratio (SNR) and minimal cross talk with scattering signatures, particularly with increasing inclusion depth.

3.2 Absolute Quantification of Optical Parameters

Recovered and expected optical parameters for Intralipid phantoms, serially diluted with porcine blood and extracted from the scaled-Monte Carlo LUT, are plotted in Fig. 6(a) and 6(d). The reduced scattering coefficient was systematically underestimated (on average, by 26%), but relative trends in the spectral scattering amplitude and slope were conserved. Systematic error in the absolute quantification of scattering was likely influence by the assumed optical parameters of the calibration phantoms, which for Intralipid, was derived by Michels[42] using Mie theory and a different acquisition geometry. Spectral
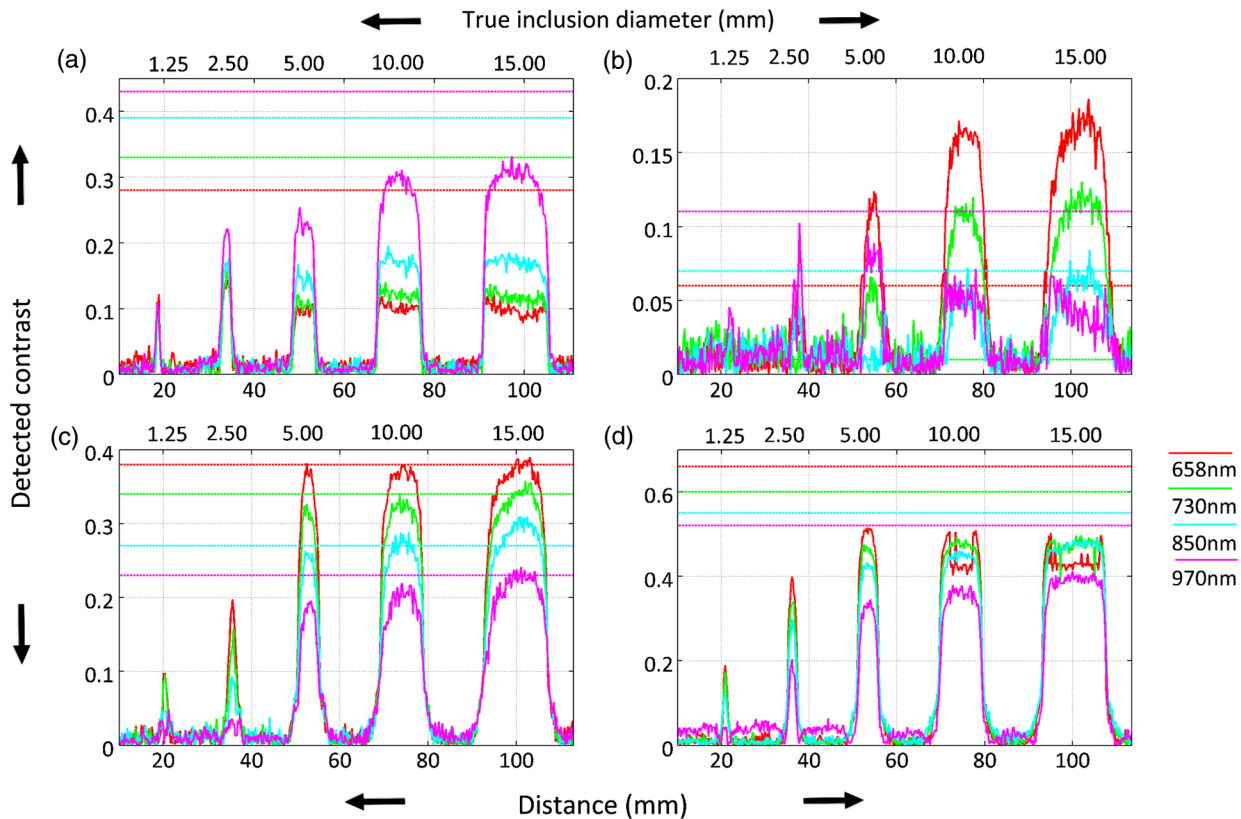

Fig. 3 (a)–(d) Detected contrast in reduced scattering maps for each contrast detail phantom per wavelength (indicated by color); scattering contrast is plotted along the center x-axis of each phantom. Expected scattering contrast per wavelength indicated by dashed line.
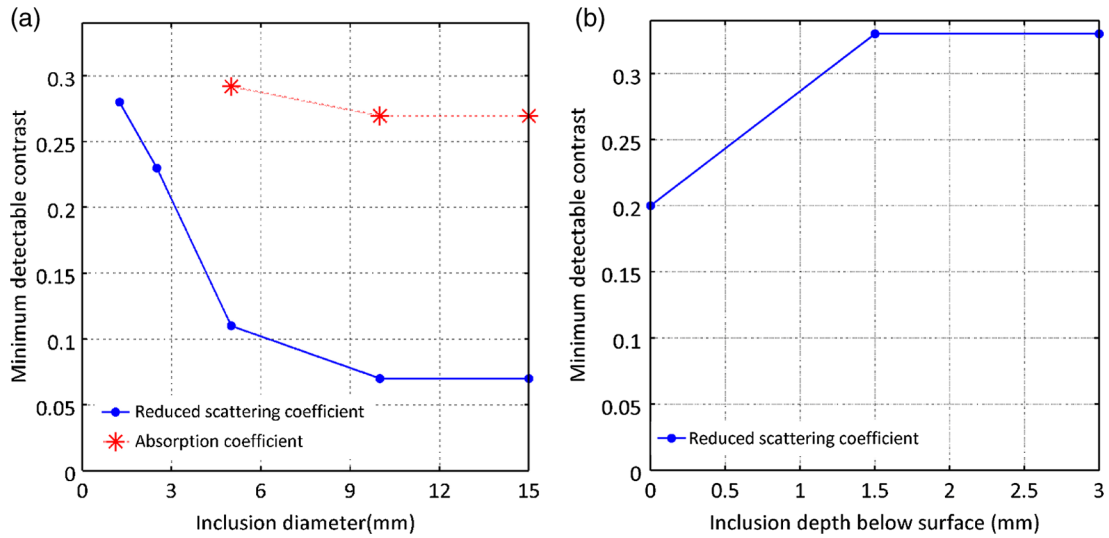
Fig. 4 (a) Minimum detectable scattering contrast plotted as a function of inclusion diameter for the reduced scattering coefficient and absorption coefficient. (b) Minimum detectable scattering contrast plotted as a function of inclusion depth for the reduced scattering coefficient. Absorption contrast was not detectable for inclusion diameters less than 5 mm in these phantoms.
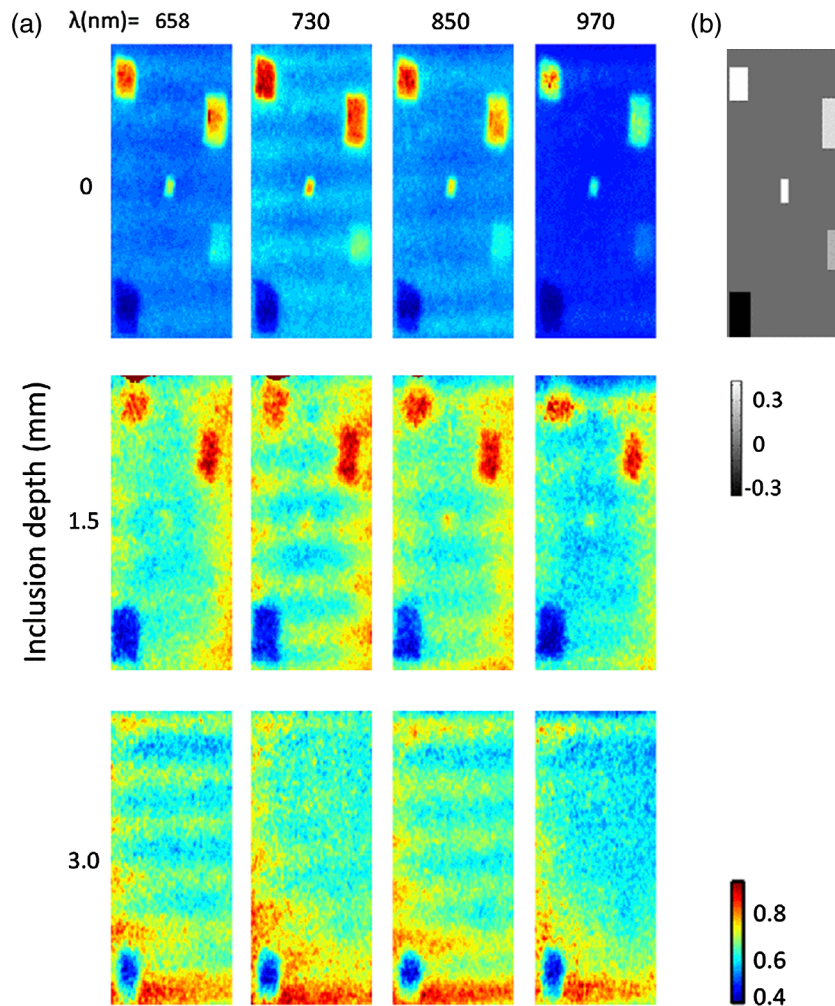

Fig. 5 (a) Reduced scattering maps (mm^{-1}) as a function of wavelength and depth for a gelatin phantom with true scattering contrast illustrated in (b) and homogenous absorption (0.005 mm^{-1}).
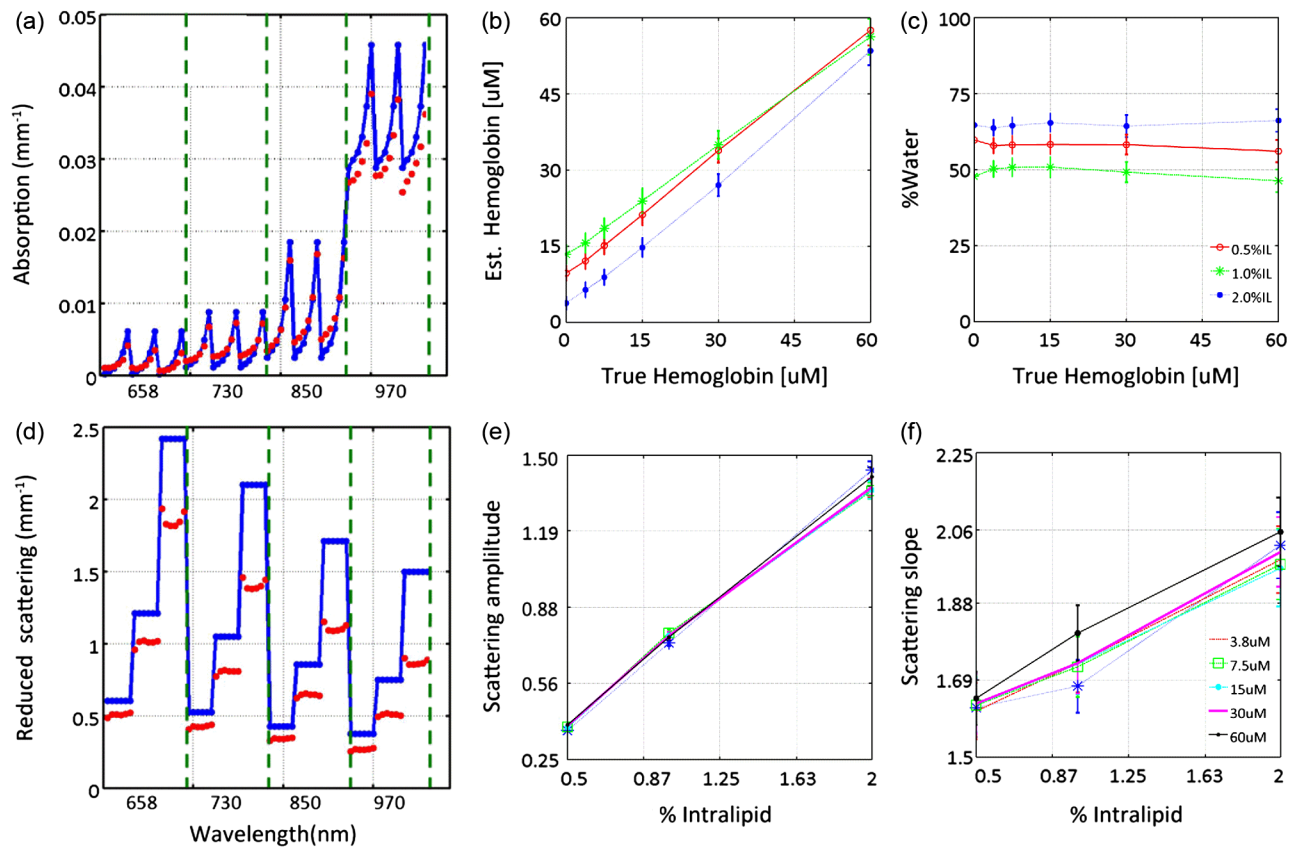
Fig. 6 (a) and (d) True (blue) and recovered (red) absorption and reduced scattering coefficients extracted from homogeneous, tissue simulating phantoms using scaled-MC simulations as a forward model. Intralipid concentrations varied from 0.5% 1.0% and 2.0%. Hemoglobin concentrations varied from 0 to 60 uM in six serial dilutions. Parameters recovered at all four wavelengths are shown in sequence. (b) and –(c) Spectral absorption parameters mapped as a function of hemoglobin concentration at three scattering concentrations (indicated by line color). (e) and (f) Spectral scattering parameters mapped as a function of Intralipid concentration for six hemoglobin concentrations (indicated by line color). Error bars indicate the standard deviation observed per 40×40 pixel window.

parameters extracted from the NIR optical coefficients are plotted as a function of Intralipid and hemoglobin concentration in Fig. 6(b) and 6(c) as well as in 6(e) and 6(f). Recovered hemoglobin values demonstrated insensitivity to scattering variations except at low concentrations and were within $+/-12\%$ of their expected values. The absorption coefficient was overestimated at visible wavelengths for low hemoglobin concentrations (<15 uM) because of the shorter pathlengths sampled. Water quantification was independent of hemoglobin changes and oxygenation levels approached 100% for all liquid phantoms (data not shown). Systematic under-estimation of absorption parameters at 970 nm was observed, likely due to the assumptions about the expected water absorption in the phantoms. Errors in Fourier Sampling theory may have also contributed minimally to amplitude underestimation, and consequently absorption overestimation, at low spatial frequencies.[1] The scattering coefficient demonstrated insensitivity to hemoglobin variations, except at the measured concentration limits (0 and 60 μM). The scattering amplitude increased linearly with scattering concentration (low coefficient of variation with Intralipid concentration: 0.26), but the scattering slope depended on both the particle size and number density (high coefficient of variation with Intralipid concentration: 1.36). All recovered absorption and scattering parameters showed strong correlation with their expected values (>0.97).

3.3 Forward Model Selection

Table 1 compares the diffusion approximation and scaled-Monte Carlo simulations of light transport according to model-data goodness of fit in a large cohort of surgical breast tissues. Three variations of the diffusion approximation were explored: a spectrally unconstrained model (a) and two spectrally constrained models (b) and (c), whose optimized parameters are listed in Table 4.2, to investigate the dependence of GOF on spectral constraints. The reduced scattering and absorption coefficients were constrained, respectively, to a power law dependence on wavelength and exponential extinction according to tabulated chromophores. Model (c) implements the most severe spectral constraints by linking the total concentration of hemoglobin to oxygen saturation (bounded between 0% and 100%) during optimization. GOF decreased with increasing spectral constraints, likely due to sparse spectral sampling. The R^2 coefficient of determination shows that the spectrally unconstrained diffusion model and scaled-Monte Carlo model performed comparably with regards to model-data goodness of fit, however the lowest adjusted-AIC suggests that the scaled-Monte Carlo model best minimized information loss in this population of surgical tissues. The correlation between the recovered and expected absorption and reduced scattering coefficients was greater than 0.97 for all models; however their coefficient of variation (CV) indicated some exponential trends in absorption

Table 1 Goodness of fit evaluated in breast tissue for three variations of the diffusion approximation and a scaled-Monte Carlo forward model, according to their average adjusted R^2 coefficient and the adjusted Akaike information criterion (AIC).

Analytical model	Optimized parameters	Adjusted R^2	Adjusted AIC
Diffusion (a)	μ_a, μ_s'	0.99	−656
Diffusion (b)	A, b, [HbO$_2$], [Hb], %H$_2$O	0.98	−616
Diffusion (c)	A, b, [HbT], %O$_2$, %H$_2$O	0.63	−343
Scaled Monte Carlo (LUT)	μ_a, μ_s'	0.99	−669

estimates with absorber concentration for both the diffusion (CV = 0.86) and scaled-Monte Carlo models (CV = 0.71); likely because the high spatial frequencies probed are less sensitive to the longer photon pathlengths associated with absorption. Sparse spectral sampling may have also limited the accuracy of chromophore quantification. Recovered scattering coefficients varied linearly with their expected values for both models (CV = 0.27 to 0.28). The scaled-Monte Carlo model was selected because its recovered absorption parameters varied more linearly with hemoglobin concentration in liquid phantoms within a physiologic hemoglobin range.

3.4 Challenges Associated with the Clinical Translation of SFDI

Spectroscopic images of four surgical margins are shown in Fig. 7: column A shows two wire-localized fibroadenomas (0.7 to 0.8 mm in diameter) in a fibrocystic background and column B shows four small fibroadenomas (0.2 to 0.5 cm in diameter) in an otherwise complete pathologic response to neoadjuvant chemotherapy. Column C shows a nearly complete pathologic response to chemotherapy, except one remaining high-grade tumor focus (0.2 cm) in the fibrocystic background. The lymphadenectomy associated with this partial responder is shown in column D; 11 out of 15 lymph nodes were positive for cancer. Oxygenation was the most apparent gauge of tumor response to therapy in these four lumpectomy specimens; oxygen levels in the lymph nodes filled with tumor were ∼40% lower than those observed in pathologically responsive tumors and fibroadenomas. Variation in optical parameters with time delay after excision reported by Bydlon suggest that oxygen saturation levels of hemoglobin vary nonlinearly within 30 min of resection; whereas, the reduced scattering coefficient and total hemoglobin concentration showed little change over time.[47] Consequently, oxygenation could be a valuable diagnostic parameter if imaged in the surgical cavity or immediately at the time of resection. High spectroscopic scattering was observed from fibrocystic tissues (columns A and C) and a lower scattering slope distinguished two large fibroadenomas within a fibrocystic background, as shown in column A. Water content was elevated and oxygenation levels were lower in the upper left quadrant of the partial responder (column C), suggesting that this quadrant was the site of the high-grade tumor focus. The primary challenges observed with the clinical translation of SFDI were edge artifacts, which presented as elevated absorption at the tissue edge, a typical location of tissue profile decline, and orienting spectroscopic images with pathology to validate margin status.

4 Discussion

In this paper, we investigate the ability of SFDI to discriminate superficial scattering contrast in tissue simulating phantoms and in surgical breast tissues. Higher spatial frequencies were probed to increase sensitivity to scattering by tissue ultra-structure because recent results suggest this is most reliable for tissue type discrimination,[47] and scattering was observed to display a more localized phenotype, as compared to absorption phenomena. Evaluation of scattering contrast in tissue-simulating phantoms showed that an inclusion as small as 1.25 mm in diameter was detectable for scattering contrast at least 28% and up to 7% scattering contrast was detected for a 10 mm inclusion; additionally, up to 33% scattering contrast was detectable at depths of 1.5 mm. This spatial resolution is sufficient to detect invasive cancers too large for effective eradication by radiation therapy. Accuracy of the diffusion approximation is known to be limited at high spatial frequencies by the restriction of no radiant anisotropy within the optical medium; here, the higher order approximation to the scattering phase function employed by Monte Carlo improved absorption quantification accuracy in breast tissues for near-source recovery of nondiffusive optical parameters.[48] Functional absorption parameters could complement information provided by spectroscopic scattering, but the accuracy of their quantification may be improved by increasing the density of spectral sampling in the NIR and by acquiring more data at low spatial frequencies.

Here, system analysis of SFDI highlights the depth selectivity of this planar acquisition geometry and explores the limitations of its contrast-detail resolution, model-data goodness of fit evaluated in surgical breast tissues, and the accuracy of optical parameter quantification. In the spatial frequency domain, effective attenuation, and consequently probing depth, δ_{eff}, is a product of both the effective attenuation coefficient, $\mu_{\mathrm{eff}} = \sqrt{3\mu_a(\mu_a + \mu_s')}$, and the illumination modulation frequency, f_x, such that $\mu_{\mathrm{eff}}' = [\mu_{\mathrm{eff}}^2 + (2\pi f_x)^2]^{1/2} = \frac{1}{\delta_{\mathrm{eff}}}$. Consequently, light is attenuated more rapidly at high spatial frequencies yielding superficial interrogation of the specimen. At high spatial frequencies, the transport coefficient, $\mu_{tr} = \mu_a + \mu_s'$, is the primary source of optical contrast. In the diffusion limit, this is predominantly a scattering signature. Sampling with a modulation frequency up to 0.33 mm^{-1}, we demonstrated an ability to detect up to 33% scattering contrast at the maximum depth relevant to surgical margin assessment (1.5 mm). The analytical solution to the diffusion approximation in the spatial frequency domain[1] reveals that reflectance behaves as an inverse function of the ratio, $\mu_{\mathrm{eff}}/\mu_{tr}$. Consequently, at low
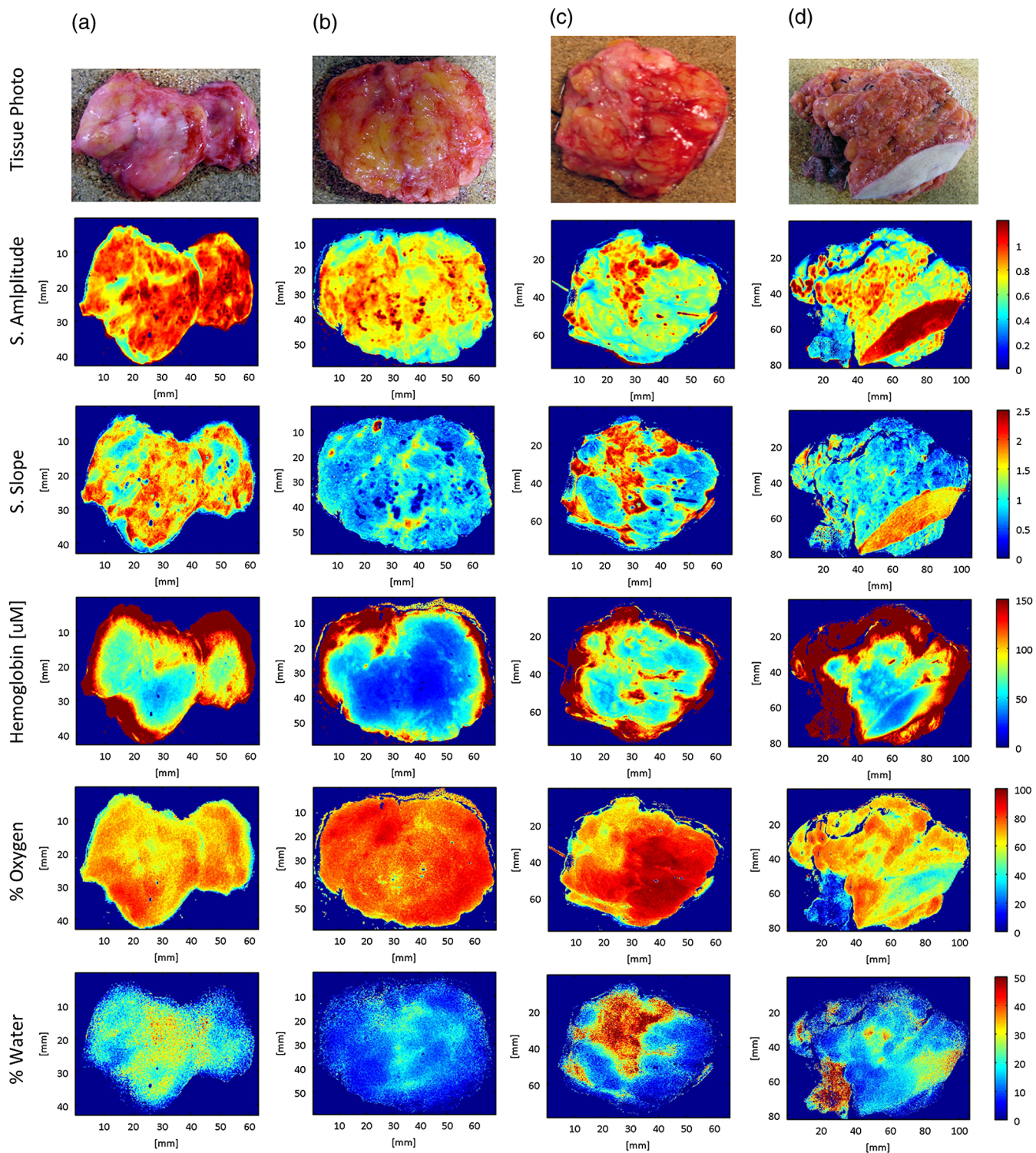
Fig. 7 Photograph and spectral parameter maps sampled from four lumpectomy margins: (a) fibroadenomas ($n = 2$) with diameters of 0.7 to 0.8 mm surrounded by fibrocystic disease, (b) complete pathologic response to neoadjuvent chemotherapy and two small fibroadenomas (diameters of 0.2 to 0.5 mm); (c) partial response to neoadjuvent chemotherapy with residual high grade tumor focus (0.2 mm) and fibrocystic disease; (d) lymphadenectomy associated with case (c). Cancer is present in 11/15 nodes. Skin and muscle in the image field appear white and deep red, respectively in the tissue photograph.

spatial frequencies, absorption dominates optical contrast and there is a relatively deeper interrogation depth. The camera resolution and the number of sources (or spatial frequencies projected per sample) additionally influence detectable contrast. Finally, absolute quantification of optical parameters requires a repeatable, stable calibration phantom with known optical properties and all measures must be made at a uniform height because the reflectance amplitude decays according to an inverse square law. A three-phase amplitude de-modulation scheme has been developed to correct for surface profile changes,[49] but continued efforts are needed to standardize calibration phantoms across institutions.

An ability to detect small foci of DCIS would be significant clinically because DCIS is typically nonpalpable and its presence critically impacts the planning of gross resection margins, a significant factor affecting long-term patient care.[50] DCIS is typified by high-grade epithelial proliferation in the lumen (which may or may not be associated with necrosis and micro-calcifications) and fibrosis in the periductal stroma.[51] It is clinically treated as a preinvasive lesion, even though it is not clear that all DCIS lesions progress to the invasive type. Contrast-detail assessment in tissue-simulating phantoms suggests that superficial clusters of DCIS, and not epithelial hyperproliferation within a single lumen, are detectable by SFDI.[52,53] However, the increased depths probed by SFDI evaluate wider margins appropriate for DCIS.

Conceivably, SFDI could readily improve resection completeness during breast conserving surgery by providing subsurface optical assessment of pathology in resected tissues. Implementation of the scaled-Monte Carlo LUT significantly reduced the computational burden associated with iterative estimation of optical parameters to render data analysis feasible in the operative setting. Data acquisition could be improved by accounting for surface profile changes during optical parameter recovery, increasing spectral resolution in the visible-NIR, and developing inking strategies that improve coregistration of spectral images with paraffin histology. Coregistration would be more feasible if the surgeon applied inks subsequent to imaging, but prior to removal of the tissue from the imaging platform. That way, inks corresponding to each image field could be recorded for pathology correlation. Precise coregistration with pathology is only necessary to validate the technology—in the surgical setting, near real-time imaging feedback would enable the surgeon to rotate the specimen and resect additional tissues as necessary. Some research groups have developed compact enclosures to maintain specimen orientation while locally sampling tissue optical properties.[54] Development of a similar device would require considerable scalability given the variation observed in resected tissue size/shape and would likely induce imaging artifacts for this illumination scheme. Edge artifacts were significantly observed in lumpectomy specimens prior to gross sectioning, but a three-phase amplitude de-modulation scheme has been developed to correct for surface profile changes[49] and will be implemented in future studies. Translation of SFDI to surgical margin assessment should focus on improving image reconstruction speed, automating combined acquisition of tissue and phantom calibration data, and developing inking strategies for improved coregistration with pathology.

5 Conclusions

The ultimate goal of conservative surgery is to remove enough primary cancer for effective eradication of microscopic residual disease by radiation therapy. Here, tissue-simulating phantoms with known properties were imaged for optimization of analysis methods to determine the microscopic sensitivity of SFDI. A 1.25 mm diameter inclusion was detectable when scattering contrast was at least 28%; a quarter of this scattering contrast (7%) was detectable for 10 mm inclusions and at least 33% scattering contrast was detected up to 1.5 mm in depth. Relative trends in the spectral scattering amplitude and slope were conserved and recovered scattering parameters demonstrated insensitivity to hemoglobin changes. Recovered hemoglobin concentrations demonstrated insensitivity to changes in scattering, except at

low hemoglobin concentrations ($<15\,\mu$M), where they were overestimated at visible wavelengths, but within 12% of their true range. The scattering amplitude increased linearly with scattering concentration, but the scattering slope depended on both the particle size and number density. Absorption parameters extracted using scaled-Monte Carlo simulations of light transport varied most linearly with expected hemoglobin concentration in liquid phantoms and minimized information loss when fitting reflectance spectra acquired from surgical breast tissues at higher spatial frequencies. Data acquisition was ultimately tested in four fully intact, lumpectomy tissues and a workflow was established for acquisition and analysis to facilitate the clinical translation of this technology to breast conserving surgery. The primary challenges observed with the clinical translation of SFDI were: edge artifacts induced by tissue surface profile changes and orienting spectroscopic images with pathology to validate margin status; these may be overcome by surface profile correction algorithms and inking strategies coordinated with the surgeon. SFDI has the potential to effectively detect tissue subtypes in surgical breast lesions because it maintains sensitivity to local scattering contrast over a wide field and data is acquired in a noncontact geometry.

References

1. D. J. Cuccia et al., "Quantitation and mapping of tissue optical properties using modulated imaging," *J. Biomed. Opt.* **14**(2), 024012 (2009).
2. T. H. Pham et al., "Quantifying the properties of two-layer turbid media with frequency-domain diffuse reflectance," *Appl. Opt.* **39**(25), 4733–4745 (2000).
3. M. Canpolat and J. R. Mourant, "Particle size analysis of turbid media with a single optical fiber in contact with the medium to deliver and detect white light," *Appl. Opt.* **40**(22), 3792–3799 (2001).
4. L. T. Perelman et al., "Observation of periodic fine structure in reflectance from biological tissue: a new technique for measuring nuclear size distribution," *Phys. Rev. Lett.* **80**(3), 627–630 (1998).
5. R. L. P. van Veen et al., "Optical biopsy of breast tissue using differential path-length spectroscopy," *Phys. Med. Biol.* **50**(11), 2573–2581 (2005).
6. P. Thueler et al., "*In vivo* endoscopic tissue diagnostics based on spectroscopic absorption, scattering, and phase function properties," *J. Biomed. Opt.* **8**(3), 495–503 (2003).
7. R. Reif, O. A'Amar, and I. J. Bigio, "Analytical model of light reflectance for extraction of the optical properties in small volumes of turbid media," *Appl. Opt.* **46**(29), 7317–7328 (2007).
8. J. R. Mourant et al., "Influence of the scattering phase function on light transport measurements in turbid media performed with small source-detector separations," *Opt. Lett.* **21**(7), 546–548 (1996).
9. F. Bevilacqua and C. Depeursinge, "Monte Carlo study of diffuse reflectance at source-detector separations close to one transport mean free path," *J. Opt. Soc. Am. A* **16**(12), 2935–2945 (1999).
10. F. Nguyen et al., "Intraoperative evaluation of breast tumor margins with optical coherence tomography," *Cancer Res.* **69**(22), 8790–8796 (2009).

11. J. Brown et al., "Quantitative optical spectroscopy: a robust tool for direct measurement of breast cancer vascular oxygenation and total hemoglobin content *in vivo*," *Cancer Res.* **69**(7), 2919–2926 (2009).

12. I. Bigio et al., "Diagnosis of breast cancer using elastic-scattering spectroscopy: preliminary clinical results," *J. Biomed. Opt.* **5**(2), 221–228 (2000).

13. B. W. Pogue et al., "Quantitative hemoglobin tomography with diffuse near-infrared spectroscopy: pilot results in the breast," *Radiol.* **218**(1), 261–266 (2001).

14. S. Srinivasan et al., "Interpreting hemoglobin and water concentration, oxygen saturation, and scattering measured *in vivo* by near-infrared breast tomography," *Proc. Natl. Acad. Sci. U.S.A.* **100**(21), 12349–12354 (2003).

15. S. Srinivasan et al., "Near-infrared characterization of breast tumors *in vivo* using spectrally-constrained reconstruction," *Technol. Cancer Res. Treat.* **4**(5), 513–526 (2005).

16. L. O. Svaasand et al., "Reflectance measurements of layered media with diffuse photon-density waves: a potential tool for evaluating deep burns and subcutaneous lesions," *Phys. Med. Biol.* **44**(3), 801–813 (1999).

17. J. R. Mourant et al., "Mechanisms of light scattering from biological cells relevant to noninvasive optical-tissue diagnostics," *Appl. Opt.* **37**(16), 3586–3593 (1998).

18. A. Kienle, F. K. Forster, and R. Hibst, "Influence of the phase function on determination of the optical properties of biological tissue by spatially resolved reflectance," *Opt. Lett.* **26**(20), 1571–1573 (2001).

19. T. J. Farrell, M. S. Patterson, and B. Wilson, "A diffusion theory model of spatially resolved, steady-state diffuse reflectance for the noninvasive determination of tissue optical properties *in vivo*," *Med. Phys.* **19**(4), 879–888 (1992).

20. N. Dognitz and G. Wagnieres, "Determination of tissue optical properties by steady-state spatial frequency-domain reflectometry," *Laser. Med. Sci.* **13**(1), 55–65 (1998).

21. A. Kim et al., "A fiberoptic reflectance probe with multiple source-collector separations to increase the dynamic range of derived tissue optical absorption and scattering coefficients," *Opt. Express* **18**(6), 5580–5594 (2010).

22. J. Sun et al., "Influence of fiber optic probe geometry on the applicability of inverse models of tissue reflectance spectroscopy: computational models and experimental measurements," *Appl. Opt.* **45**(31), 8152–8162 (2006).

23. J. C. Finlay and T. H. Foster, "Hemoglobin oxygen saturations in phantoms and *in vivo* from measurements of steady-state diffuse reflectance at a single, short source-detector separation," *Med. Phys.* **31**(7), 1949–1959 (2004).

24. R. Graaff et al., "Condensed Monte Carlo simulations for the description of light transport," *Appl. Opt.* **32**(4), 426–434 (1993).

25. A. Kienle and M. S. Patterson, "Determination of the optical properties of turbid media from a single Monte Carlo simulation," *Phys. Med. Biol.* **41**(10), 2221–2227 (1996).

26. R. Pleijhuis et al., "Obtaining adequate surgical margins in breast-conserving therapy for patients with early-stage breast cancer: current modalities and future directions," *Ann. Surg. Oncol.* **16**(10), 2717–2730 (2009).

27. "Cancer Facts and Figures," American Cancer Society (2011).

28. U. Veronesi et al., "Twenty-year follow-up of a randomized study comparing breast-conserving surgery with radical mastectomy for early breast cancer," *New Engl. J. Med.* **347**(16), 1227–1232 (2002).

29. B. Fisher et al., "Twenty-year follow-up of a randomized trial comparing total mastectomy, lumpectomy, and lumpectomy plus irradiation for the treatment of invasive breast cancer," *New Engl. J. Med.* **347**(16), 1233–1241 (2002).

30. C. D. Scopa et al., "Evaluation of margin status in lumpectomy specimens and residual breast carcinoma," *Breast J.* **12**(2), 150–153 (2006).

31. S. J. Schnitt et al., "The relationship between microscopic margins of resection and the risk of local recurrence in patients with breast cancer treated with breast-conserving surgery and radiation therapy," *Cancer* **74**(6), 1746–1751 (1994).

32. B. Spivack et al., "Margin status and local recurrence after breast-conserving surgery," *Arch. Surg.-Chicago* **129**(9), 952–956 (1994).

33. M. Clarke et al., "Effects of radiotherapy and of differences in the extent of surgery for early breast cancer on local recurrence and 15-year survival: an overview of the randomised trials," *Lancet* **366**(9503), 2087–2106 (2005).

34. J. Ferreiro, J. Gisvold, and D. Bostwick, "Accuracy of frozen section diagnosis of mammographically detected breast biopsies; results of 1,490 consecutive cases," *Am. J. Surg. Path.* **19**(11), 1267–1271 (1995).

35. J. Tinnemans, T. Wobbes, and R. Holland, "Mammographic and histopathologic correlation of non-palpable lesions of the breast and reliability of frozen section diagnosis," *Surg. Gynecol. Obstet.* **165**(6), 523–529 (1987).

36. G. Gibson et al., "A comparison of ink-directed and traditional whole cavity re-excision for breast lumpectomy specimens with positive margins," *Ann. Surg. Oncol.* **8**(9), 693–704 (2001).

37. D. J. Cuccia et al., "Modulated imaging: quantitative analysis and tomography of turbid media in the spatial-frequency domain," *Opt. Lett.* **30**(11), 1354–1356 (2005).

38. M. A. A. Neil, R. Juskaitis, and T. Wilson, "Method of obtaining optical sectioning by using structured light in a conventional microscope," *Opt. Lett.* **22**(24), 1905–1907 (1997).

39. F. Bevilacqua et al., "Broadband absorption spectroscopy in turbid media by combined frequency-domain and steady-state methods," *Appl. Opt.* **39**(34), 6498–6507 (2000).

40. A.-N. Spiess and N. Neumeyer, "An evaluation of R2 as an inadequate measure for nonlinear models in pharmacological and biochemical research: a Monte Carlo approach," *BMC Pharmacol.* **10**(6) (2010).

41. H. Akaike, "New look at statistical model identification," *IEEE Trans. Autom. Control* **19**(6), 716–723 (1974).

42. R. Michels, F. Foschum, and A. Kienle, "Optical properties of fat emulsions," *Opt. Express* **16**(8), 5907–5925 (2008).

43. A. Mazhar et al., "Wavelength optimization for rapid chromophore mapping using spatial frequency domain imaging," *J. Biomed. Opt.* **15**(6), 061716 (2010).

44. S. L. Jacques and S. Prahl, *Optical Properties Spectra*, Oregon Medical Laser Center, Portland, Oregon (2010).

45. B. W. Pogue and M. S. Patterson, "Review of tissue simulating phantoms for optical spectroscopy, imaging and dosimetry," *J. Biomed. Opt.* **11**(4), 041102 (2006).

46. B. Pogue et al., "Characterization of hemoglobin, water, and NIR scattering in breast tissue: analysis of intersubject variability and menstrual cycle changes," *J. Biomed. Opt.* **9**(3), 541–552 (2004).

47. T. M. Bydlon et al., "Advancing pptical imaging for breast margin assessment: an analysis of excisional time, cautery, and patent blue dye on underlying sources of contrast," *PLoS One* **7**(12), e51418 (2012).

48. S. D. Konecky et al., "Imaging scattering orientation with spatial frequency domain imaging," *J. Biomed. Opt.* **16**(12), 126001 (2011).

49. S. Gioux et al., "Three-dimensional surface profile intensity correction for spatially modulated imaging," *J. Biomed. Opt.* **14**(3), 034045 (2009).

50. W. A. Wells et al., "Phase contrast microscopy analysis of breast tissue differences in benign vs. malignant epithelium and stroma," *Anal. Quant. Cytol. Histol.* **31**(4), 197–207 (2009).

51. E. B. Claus et al., "Prevalence of BRCA1 and BRCA2 mutations in women diagnosed with ductal carcinoma *in situ*," *JAMA J. Am. Med. Assoc.* **293**(8), 964–969 (2005).

52. A. M. Laughney et al., "Scatter spectroscopic imagin distinguishes breast pathologies in tissues relevant to surgical margin assessment," *Clin. Cancer Res.* **18**(22), 6315–6325 (2012).

53. A. M. Laughney et al., "Automated classification of breast pathology using local measures of broadband reflectance," *J. Biomed. Opt.* **15**(6), 066019 (2010).

54. J. Q. Brown et al., "Intraoperative optical breast tissue characterization device for tumor margin assessment," *Cancer Res.* **69**(2), 101s–101s (2009).